

Constraints to the magnetospheric properties of T Tauri stars - I. The C II], Fe II] and Si II] ultraviolet features

Fatima López-Martínez¹ ^{*} and Ana Inés Gómez de Castro¹ [†]

¹*AEGORA Research Group, Universidad Complutense de Madrid, Plaza de Ciencias 3, 28040 Madrid, Spain*

Submission, February XXth, 2014

ABSTRACT

The C II] feature at ~ 2325 Å is very prominent in the spectra of T Tauri stars (TTs). This feature is a quintuplet of semiforbidden transitions excited at electron temperatures around 10,000 K that, together with the nearby Si II] and Fe II] features, provides a reliable optically thin tracer for accurate measurement of the plasma properties in the magnetospheres of TTs. The spectra of 20 (out of 27) TTs observed with the Space Telescope Imaging Spectrograph on board the *Hubble Space Telescope* have good enough signal-to-noise-ratio at the C II] wavelength. For these stars, we have determined electron densities (n_e) and temperatures (T_e) in the line emission region as well as the profile broadening (σ). For most of the stars in the sample (17) we obtain $10^{4.1} \lesssim T_e \lesssim 10^{4.5}$ K and $10^8 \lesssim n_e \lesssim 10^{12}$ cm⁻³. These stars have suprathermal line broadening ($35 \lesssim \sigma \lesssim 165$ km s⁻¹), except TW Hya and CY Tau with thermal line broadening. Both C II] line luminosity and broadening are found to correlate with the accretion rate. Line emission seems to be produced in the magnetospheric accretion flow, close to the disc. There are three exceptions: DG Tau, RY Tau and FU Ori. The line centroids are blueshifted indicating that the line emission in these three stars is dominated by the outflow.

Key words: stars: magnetic field - stars: pre-main sequence - stars: winds, outflows - ultraviolet: stars

1 INTRODUCTION

T Tauri stars (TTs) are young and low-mass ($\lesssim 3 M_\odot$) pre-main sequence stars with strong and complex magnetic fields and a surrounding disc that is truncated near the corotation radius by interaction with the magnetic field. From the observational point of view TTs are split into two main groups: Classical TTs (CTTs) and Weak lined TTs (WTTs). CTTs are accreting mass from the disc whereas WTTs have no or very little spectral signatures of accretion. The material in the inner part of the disc is ionized by the stellar radiation and channelled through the magnetic field lines (Uchida & Shibata 1984; Koenigl 1991). The gas from the disc is accelerated to almost free-fall velocity before it reaches the stellar surface forming an accretion shock (see, e.g., the reviews by Bouvier et al. 2007; Gómez de Castro 2013a). Detailed simulations of the interaction between the stellar field and the inner disc show a complex dynamics of the magnetospheric flow that depends on the field properties and its stability (Romanova et al. 2012; Kurosawa & Romanova 2013). Some analytical ex-

pressions for the hotspot shapes and the magnetospheric radius have been provided by Kulkarni & Romanova (2013).

The interaction between the star, disc and magnetic field produces an excess emission at different wavelengths that affects the evolution of the disc itself and the circumstellar environment. The atmospheric and magnetospheric energy output is released mainly in the ultraviolet (UV) spectral range. Thus, there is a relatively large number of spectral features in the UV that can be used as potential tracers of the physical conditions in TTs. Different emission lines in the UV wavelength range provide different information about the regions in which they are formed, the involved physical processes and the system geometry. For example, the Mg II resonance doublet at 2795.5 and 2802.7 Å is produced in the chromosphere of TTs and it is one of the strongest features in UV spectra of TTs. Mg II is sensitive to, and can be used as a good tracer of, atmosphere and outflow/wind in TTs (Ardila et al. 2002b; Calvet et al. 2004; Ingleby et al. 2013, López-Martínez & Gómez de Castro, submitted). N V, C IV, He II and Si IV are good tracers of hot gas and accretion processes in TTs. The relationship between these lines and mass accretion in TTs has been already studied by different authors (Johns-Krull et al. 2000; Ardila et al. 2002a; Ingleby et al. 2011; Yang et al. 2012;

^{*} E-mail: fatimalopezmar@gmail.com

[†] E-mail: aig@ucm.es

Gómez de Castro & Marcos-Arenal 2012; Ardila et al. 2013; Gómez de Castro 2013b).

The semiforbidden lines of the C II] quintuplet (wavelengths: 2324.21, 2325.4, 2326.11, 2327.64, 2328.83 Å) are not observed in WTTSSs; however, they are readily detected in CTTSSs, even in low mass accretors (Lamzin 2000). This multiplet seems to be a very sensitive tracer of accretion or outflows (Calvet et al. 2004; Gómez de Castro & Ferro-Fontán 2005; Ingleby et al. 2013). Calvet et al. (2004) and Ingleby et al. (2013) analysed these lines in low resolution spectra and found a relationship between the C II] luminosity and the accretion luminosity. The study of the C II] flux ratios within a small range of wavelengths provides a good opportunity to investigate TTS properties because they are optically thin and their ratios do not depend on the geometry of the accretion system and are only slightly affected by the large uncertainties associated with extinction determination. It is known that the relative intensities of the emission lines of the C II] multiplet are sensitive to the electron density in the range $10^8 \lesssim n_e \lesssim 10^{10} \text{ cm}^{-3}$ (Stencel et al. 1981; Hayes & Nussbaumer 1984a,b; Keenan et al. 1986). Plasma in the magnetospheres and atmospheres of CTTSSs is within this density range. However, line blending makes it difficult to identify the individual features and to measure the lines ratios (see, e.g. Lamzin 2000; Kravtsova & Lamzin 2002, observations of RU Lup and DR Tau, respectively).

In this work, we present for the first time a study of C II] line ratios in a sample of 20 CTTSSs using 30 medium-resolution spectra. We found the best-fitting spectrum to the data using a grid of simulated profiles computed for a broad range of electron densities and temperatures. The log of observations, the characteristics of the CTTSSs sample and the profiles are described in Section 2. The numerical method used to derive the individual lines fluxes and the properties of the radiating plasma is presented in Section 3, that also includes the limitations of the method and the final results. In Section 4, we present the plasma properties obtained with our procedure and they are compared with the accretion rates derived from Ingleby et al. (2013). To conclude, in Section 5, we provide a brief summary of the main results.

2 THE C II] PROFILE OF CTTSS

Our sample consists of the 27 CTTSSs observed with the Space Telescope Imaging Spectrograph (STIS) on board the *Hubble Space Telescope* (HST); no C II] emission is detected in WTTSSs. Most of the sources (17 of 27) are located in Taurus-Auriga Molecular Cloud. The rest of the sources are in η Chamaleon (2), ϵ Chamaleon (1), Chamaleon I (2), TW Hydra Association (2), Orion (1) and Upper Scorpius (1). DK Tau, HN Tau (Correia et al. 2006), CV Cha (Bary et al. 2008) and UX Tau (Nguyen et al. 2012) are binaries with companions at distances of 2.304, 3.109, 11.4 and 5.9 arcsec, respectively, that are resolved by STIS. T Tau (Furlan et al. 2006), FU Ori (Wang et al. 2004) and DF tau (Unruh et al. 1998) are close binaries at distances 0.7, 0.5 and 0.09 arcsec, respectively. CS Cha is a spectroscopic binary (Guenther et al. 2007). Several stars show evidence of transitional discs, but they are still accreting: CS Cha,

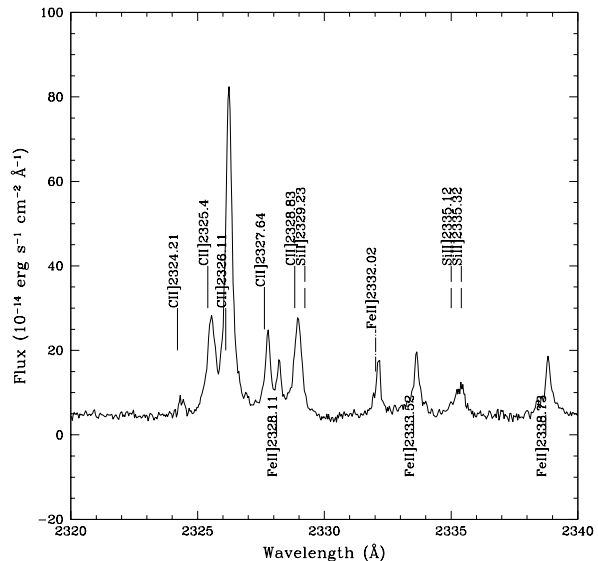


Figure 2. Line identification in the spectral range 2320-2340 Å on TW Hya spectrum.

DM Tau, GM Aur, TW Hya and UX Tau (Espaillat et al. 2010). In some sources of our sample jets/outflows have been detected: RY Tau (St-Onge & Bastien 2008), DG Tau (Coffey et al. 2008), T Tau (Furlan et al. 2006), SZ 102 (Comerón & Fernández 2011), AA Tau, DF Tau, HN Tau and SU Aur (Howard et al. 2013).

The sample is formed of 42 medium-resolution ($R \simeq 30000$) spectra obtained with grating E230M; the log of data is provided in Table 1. We have selected spectra with signal-to-noise-ratio (S/N) > 2 ; the S/N has been calculated over the whole feature as described in Section 3.3. The spectra are shown in Fig. 1. No significant variations are detected in the spectrum of sources with multiple observations, except for DS Tau (see Appendix A); note that though the C II] flux of DS Tau drops by a factor of 2 between two observations, no significant profile shape variations are noticeable.

In Fig.2, the main spectral features in the 2324-2336 Å range are indicated on the spectrum of TW Hya, the star with the best S/N in the sample. Note that the C II] multiplet is resolved. Additional relevant features in the range are:

- (i) The Fe II] lines at 2328.11 and 2333.52 Å ($3d^6(^5D)4s - 3d^6(^5D)4p$). Note that the 2328.11 Å transition is blended with the C II] lines in most spectra.
- (ii) The Fe II] lines at 2332.02 and 2333.52 Å.
- (iii) The Si II] multiplet at 2329.23, 2335.12 and 2335.32 Å.

3 MEASURING THE PLASMA PROPERTIES

C II], Fe II] and Si II] features are intercombination transitions with very small Einstein coefficients and thus, optically thin tracers of the radiating plasma, suitable to be used to measure directly their properties. This characteristic was already noticed by Stencel et al. (1981) for C II]

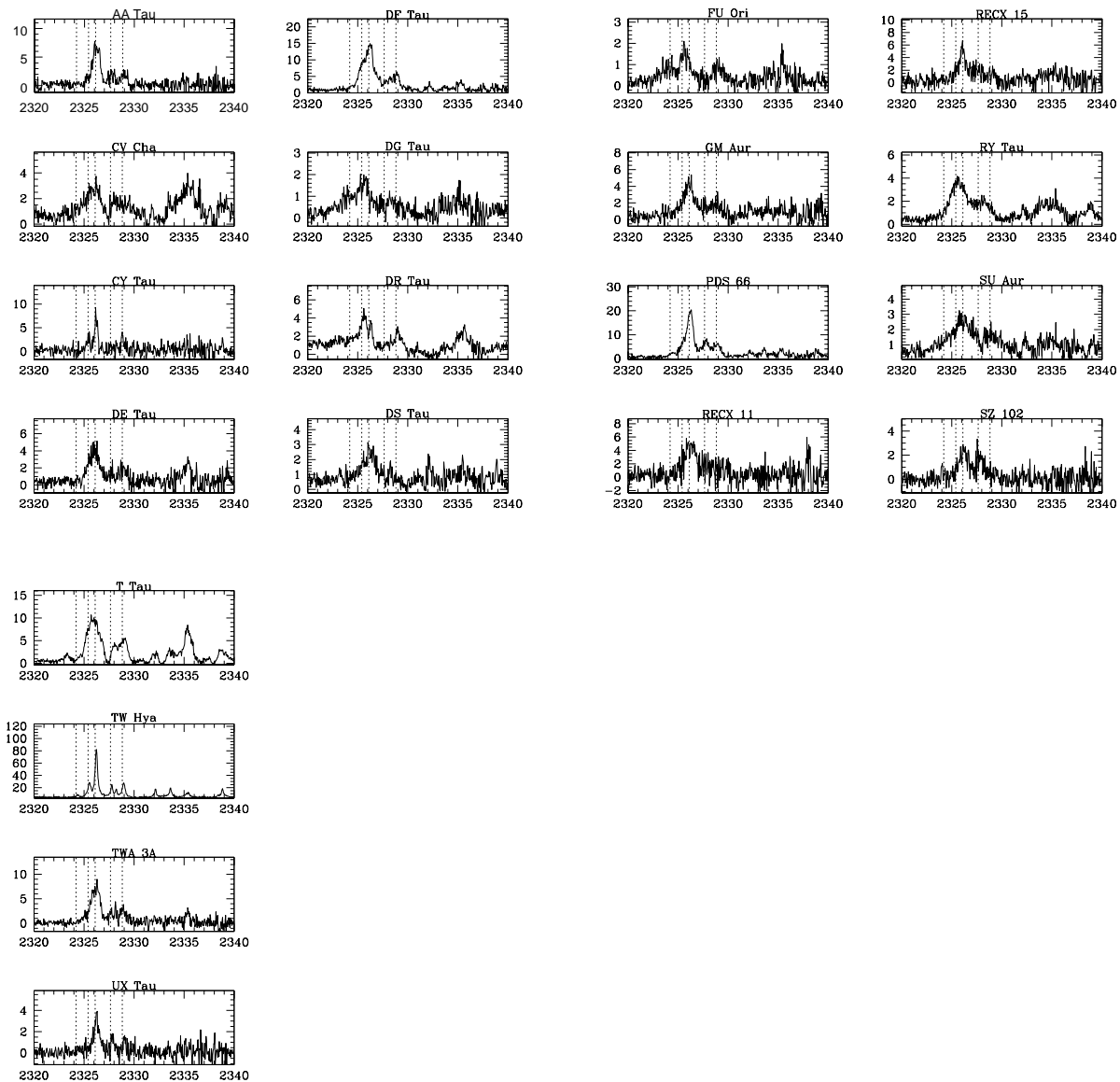


Figure 1. The C II] multiplet in the TTSs; only profiles with $S/N > 2$ are plotted. The fluxes are in units of $10^{-14} \text{ erg s}^{-1} \text{ cm}^{-2} \text{ Å}^{-1}$. Dashed lines mark the rest wavelengths of the C II] transitions. For stars with multiple observations, the spectrum with the best S/N is shown.

lines, who proposed to use them as electron density tracers in the $10^7 \leq n_e \leq 10^{10.5} \text{ cm}^{-3}$ range in nebulae research. In Fig.3, we display the sensitivity of the line ratios to T_e and n_e for this quintuplet. The plot was made by using the Atomic Database for Spectroscopic Diagnostics of Astrophysical Plasmas CHIANTI¹ (Dere et al. 1997; Landi et al. 2013). Note that below $n_e \leq 10^8 \text{ cm}^{-3}$, the ratios are insensitive to the electron density except for very diffuse plasmas with $n_e \lesssim 10^{2.5} \text{ cm}^{-3}$. Therefore, other species need to be considered to constrain the T_e of the plasma and the density for $n_e \gtrsim 10^{10.5} \text{ cm}^{-3}$ and $n_e \lesssim 10^8 \text{ cm}^{-3}$. The Fe II] ratios are sensitive to the electron density for $n_e \gtrsim 10^9 \text{ cm}^{-3}$

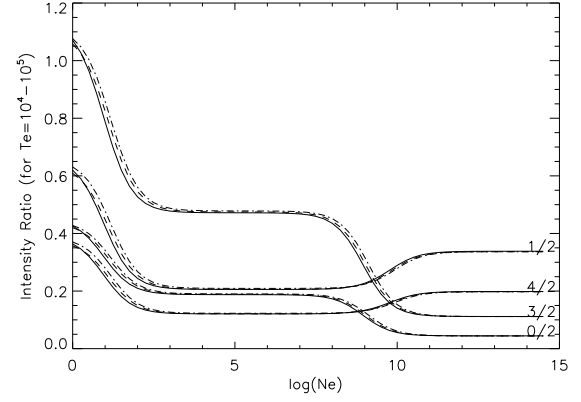
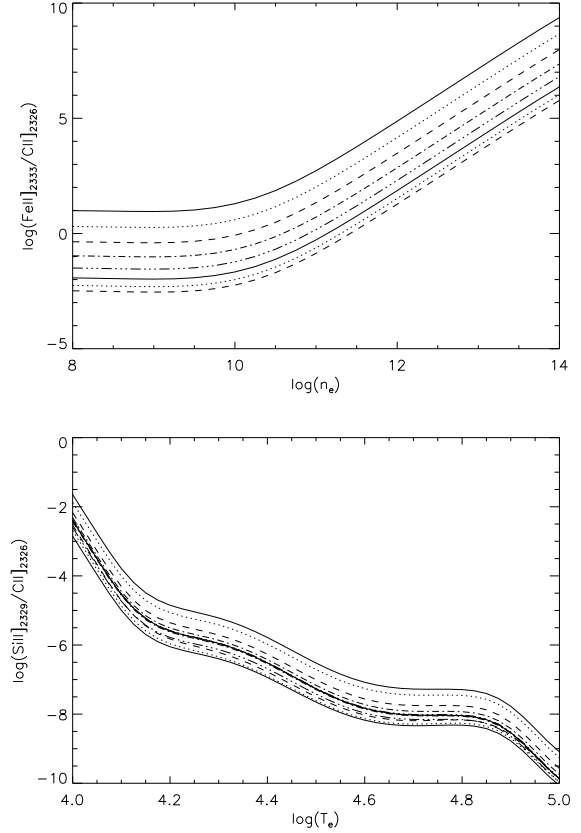
(see top panel in Fig.4), the range of densities for which the C II] quintuplet ratios are nearly constant. The Si II] ratios are more sensitive to the temperature, particularly for $T_e \lesssim 10^{4.5} \text{ K}$ (see bottom panel in Fig.4). The combined analysis of all these ratios yields enough information to determine unambiguously the physical properties of the region where the lines are formed.

For the calculations, we have assumed that all the lines are optically thin and formed via collisional excitation in a single plasma characterized by a pair (n_e, T_e) . CHIANTI provides the ion emissivities (erg s^{-1}): $\varepsilon_{ij} = \Delta E (n_j(\text{XII})/n(\text{XII})) A_{ji}$, being ΔE the difference of energies between levels j and i , $n_j(\text{XII})/n(\text{XII})$ the fraction of ions lying in the state j and A_{ji} the spontaneous radiative transition probability. The emissivities per unit volume

¹ www.chiantidatabase.org

Table 1. Log of observations.

Star	Obs date (yy/mm/dd)	Data set	Exp time (s)	S/N
AA Tau	11/01/07	ob6ba7030	1462.2	3.21
CS Cha	11/06/01	ob6bb6030	1785.2	1.65
CV Cha	11/04/13	ob6b18020	2598.2	3.30
CY Tau	00/12/06	o5cf03020	738	2.54
	00/12/06	o5cf03030	282	1.75
DE Tau	10/08/20	ob6ba8030	1388.1	3.58
DF Tau	99/09/18	o5kc01020	1670.2	14.72
DG Tau	01/02/20	o63l03010	2345	1.87
	01/02/20	o63l03020	2923	2.66
	01/02/20	o63l03030	2923	2.56
	01/02/20	o63l03040	2923	1.91
DK Tau	10/02/04	ob6bb2030	854.4	0.81
DM Tau	10/08/22	ob6ba2030	1330.1	1.37
DN Tau	11/09/10	ob6ba4030	1441.2	1.72
DR Tau	00/08/29	o5cf02020	916	1.12
	01/02/09	o63l04010	2327	2.04
	01/02/09	o63l04020	2880	2.26
	10/02/15	ob6bb4030	881.3	0.44
DS Tau	00/08/24	o5cf01020	878	2.06
	01/02/23 ^(g)	o63l08010	2345	2.27
	01/02/23	o63l08020	2923	2.12
FM Tau	11/09/21	ob6ba0030	1401.2	0.64
FU Ori	01/02/22	o63l07020	2880	2.54
GM Aur	10/08/19	ob6ba1030	1300.5	3.61
HN Tau	10/02/10	ob6ba9030	807.5	1.24
PDS 66	11/05/23	ob6b23030	1725.2	11.68
RECX15	10/02/05	ob6bb7030	916.4	2.45
RECX11	09/12/12	ob6bc4030	697.8	2.32
RY Tau	01/02/19	o63l01010	2353	7.47
	01/02/20	o63l01020	2923	8.09
	01/02/20	o63l01030	2923	7.92
SU Aur	01/02/24	o63l05010	2383	5.04
	01/02/24	o63l05020	2940	4.21
	11/03/25	ob6bb1030	1489.2	2.33
SZ 102	11/05/29	ob6bb9030	1469.2	3.12
T Tau	01/02/21	o63l02010	2331	12.57
	01/02/21	o63l02020	2880	13.95
	01/02/22	o63l02030	2880	13.53
TW Hya	00/05/07	o59d01020	1675.2	21.23
TWA 3A	11/03/26	ob6b22030	1107.2	6.70
UX Tau	11/11/10	ob6b54030	1408.2	2.35
V836 Tau	11/02/05	ob6ba6030	1396.2	0.64

**Figure 3.** Emissivity ratios of the C II] lines relative to the 2326.11 Å line, as a function of electron density. The labels 0,1,2,3 and 4 correspond to the C II] lines 2324, 2325, 2326, 2327 and 2328 Å, respectively. Solid, dashed and dotted lines correspond to temperatures of $T_e = 10^4$, $10^{4.5}$ and $T_e = 10^5$ K, respectively.**Figure 4.** Top panel: emissivity ratios of the Fe II] line relative to the C II] 2326.11 Å line as a function of density for several temperatures (from $\log T_e(\text{K}) = 4.0$ to 4.175 in steps of 0.025). Bottom panel: emissivity ratios of the Si II] line relative to the C II] 2326.11 Å line as a function of temperature for several densities (from $\log n_e(\text{cm}^{-3}) = 0.0$ to 13.0 in steps of 1.0).

(erg s⁻¹ cm⁻³) for a given ion X II have been calculated as:

$$\begin{aligned}\epsilon_{ij} &= \Delta E n_j(\text{XII}) A_{ji} \\ &= \Delta E A_{ji} \left(\frac{n_j(\text{XII})}{n(\text{XII})} \frac{n(\text{XII})}{n(\text{X})} \frac{n(\text{X})}{n(\text{H})} \frac{n(\text{H})}{n_e} n_e \right) \\ &= \epsilon_{ij} \left(\frac{n(\text{XII})}{n(\text{X})} \frac{n(\text{X})}{n(\text{H})} \frac{n(\text{H})}{n_e} n_e \right),\end{aligned}$$

where $n_j(\text{XII})$ is the number density of the specie X II in the upper level (j), $n(\text{XII})/n(\text{X})$ is the ionization fraction of X and $n(\text{X})/n(\text{H})$ is the abundance of element X. Solar metallicity is assumed. $n(\text{H})/n_e = 0.83$ has been used since $T_e > 10^4$ K (see CHIANTI manual).

3.1 The numerical method

Making use of the emissivities from CHIANTI, we have computed the flux ratios relative to the C II] (2326.11 Å) line of the following lines: C II] (2324.21, 2325.4, 2327.64 and 2328.83 Å), Fe II] (2328.11 and 2333.52 Å), Fe II] (2332.02 Å) and Si II] (2329.23, 2335.12 and 2335.32 Å), for a grid of electron temperatures and densities. The grid covers the range $4.0 \leq \log T_e(\text{K}) \leq 5.5$ and $0.0 \leq \log n_e(\text{cm}^{-3}) \leq 14.5$ with resolutions 0.025 dex in $\log(T_e)$ and 0.25 dex in $\log(n_e)$. We have assumed that the lines profiles are adequately reproduced by Gaussian functions. In this manner, we have built a grid of simulated spectra in the 2323-2338 Å spectral range given by

$$F(\lambda) = F_0 \sum_{i=0}^{10} R_i \exp\left(\frac{-(\lambda - (\lambda_i + \delta))^2}{2\sigma^2}\right) + F_{cont}, \quad (1)$$

where F_0 is the peak flux of the reference line (C II]2326), $R_i = F_i/F_0$ is the flux ratio between the peak of the i th line and F_0 , σ is the standard deviation of the Gaussian functions and λ_i is the central wavelength of the i th emission line (which can be shifted δ Å from its expected position). F_{cont} is directly computed from the observations as the average flux in the 2320-2323 Å range for each spectra; this is a featureless window (see Fig.1). Both dispersion (σ) and shift (δ) are assumed to be the same for all lines.

We developed an IDL based code to identify the synthetic spectrum that best fit the data consisting in two main steps. First, for each synthetic spectrum - defined by a pair (n_e, T_e) - the best fit to the data is found by a least squares scheme that leaves F_0 , δ and σ as free parameters for the fit. As a result, for any given model i ($n_{e,i}$, $T_{e,i}$), the set of parameters that best fit the data ($F_{0,i}$, σ_i , δ_i), as well as the residuals, χ_i^2 , are computed. This allows plotting the χ^2 surface in the (n_e, T_e) space (see Fig.5). Then, the minimum of the surface is identified providing the (n_e, T_e) pair that best fit the data. This minimum corresponds to the optimal fit, i.e. $\chi_{opt}^2 = \min(\chi^2)$. In Table 2, the n_e, T_e, σ, δ values corresponding to the best-fitting model are provided for all the TTSs in the study. Initial conditions for the free parameters are set as follows: $\sigma_0 = 0.1$ Å (approximately equivalent to the combination of the spectral resolution obtained with STIS/E230M and thermal broadening), F_0 is set as the peak flux around 2326 Å and δ_0 is such that $F(2326.11 - \delta_0) = F_0$ in the observed spectrum. We performed several tests to check the dependence of the results on the initial values of the free parameters. By varying these initial values, the final

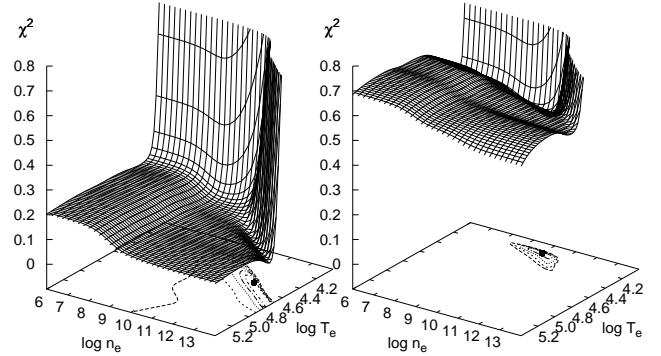


Figure 5. χ^2 surfaces and contours for TW Hya (on the left) and DE Tau (on the right). At the bottom of the figures, we projected five χ^2 contours starting close to the best solution χ_{opt}^2 (0.08 and 0.48, respectively), with steps of 0.01. The black point at the bottom indicates the T_e and n_e values finally adopted.

solution (χ_{opt}^2) never differed by more than one step in the grid of T_e and n_e values. This means that the steps of the grid represent the internal precision of the fitting procedure ($\delta \log T_e(\text{K}) \simeq 0.025$ and $\delta \log n_e(\text{cm}^{-3}) \simeq 0.25$); they are the same for all stars in the sample.

From the fitting procedure, we also estimated the uncertainties associated to δ , σ and each line flux. For this, we selected the eight closest grid points to the best fit (the local minimum) and we calculated the standard deviation from the average value using these eight points. The standard deviations in δ is always $\lesssim 5$ km s⁻¹, whereas in σ is $\lesssim 6$ km s⁻¹. These uncertainties are not provided in Table 2 because they are negligible. The final simulated fluxes with their associated errors are shown in Table 3.

The Fe II]2332.02 line has not been considered for the fit. We have found a large discrepancy between CHIANTI predictions for the line strength ($\epsilon(2332.02) \sim 0.06 \cdot \epsilon(2333.52)$) and the observations, where both Fe II lines have comparable strengths (see Fig.2).

Fig.6 shows two illustrative examples of the results of the fitting procedure. The targets selected are TW Hya, with high S/N and DE Tau with low S/N. The difference in S/N is readily observed in the χ^2 surface (see Fig.5); the height of the surface above the (n_e, T_e) plane increases as the S/N decreases. However both surfaces share some common characteristics: (1) a steep rise of the χ^2 surface towards low T_e and low n_e and (2) there is always a narrow range of (n_e, T_e) that gives the best statistical fits to the original data (see the projected contours of the χ^2 surfaces on the n_e, T_e plane in Fig.5).

3.2 (n_e, T_e) in the line emission region

Fig.7 shows the electron densities and temperatures corresponding to the optimal fits. For stars with multiple observations, only the best-fitting (with the minimum χ_{opt}^2) results are plotted. The differences among observations are

Table 2. Physical parameters derived from the fitting.

Star	Data set	$\log(T_e)$ (K)	$\log(n_e)$ (cm^{-3})	χ_{opt}^2	δ (km s^{-1})	σ (km s^{-1})	F_0 ($\text{erg s}^{-1} \text{cm}^{-2} \text{\AA}^{-1}$)
AA Tau	ob6ba7030	4.95	9.50	0.54	17.67	40.88	6.70×10^{-14}
CV Cha	ob6b18020	4.10	10.50	0.28	18.57	82.03	1.82×10^{-14}
CY Tau	o5cf03020	4.50	11.75	0.49	15.22	23.73	6.08×10^{-14}
DE Tau	ob6ba8030	4.15	10.00	0.48	0.90	56.36	3.52×10^{-14}
DF Tau	o5kc0102	4.45	11.50	0.01	9.29	66.42	1.12×10^{-13}
DG Tau	o63l03020	4.18	10.25	0.12	-67.32	104.72	9.23×10^{-15}
	o63l03030	4.15	10.00	0.13	-66.03	116.85	9.26×10^{-15}
DR Tau	o63l04010	5.48	13.75	0.42	-24.76	85.38	1.62×10^{-14}
	o63l04020	5.48	13.75	0.48	-26.70	71.97	2.02×10^{-14}
DS Tau	o5cf01020	4.35	9.75	0.75	27.34	62.03	3.72×10^{-14}
	o63l08010	4.18	9.50	0.20	19.09	62.29	1.68×10^{-14}
	o63l08020	4.18	9.50	0.15	16.77	66.03	1.74×10^{-14}
FU Ori	o63l07020	4.18	10.25	0.14	-45.53	93.89	9.12×10^{-15}
GM Aur	ob6ba1030	4.38	11.50	0.47	14.83	68.48	3.26×10^{-14}
PDS66	ob6b23030	4.30	8.75	0.01	15.35	44.88	1.79×10^{-13}
RECX15	ob6bb7030	4.15	8.50	0.86	1.42	53.91	4.28×10^{-14}
RECX11	ob6bc4030	4.40	9.00	1.53	30.82	61.00	4.31×10^{-14}
RY Tau	o63l01010	4.13	8.50	0.21	-39.34	95.95	2.64×10^{-14}
	o63l01020	4.18	10.75	0.16	-30.57	102.14	2.59×10^{-14}
	o63l01030	4.23	11.00	0.17	-25.67	110.79	2.37×10^{-14}
SU Aur	o63l05010	4.33	11.00	0.18	18.70	158.12	1.30×10^{-14}
	o63l05020	4.18	10.25	0.20	-6.84	155.80	1.38×10^{-14}
	ob6bb1030	4.18	10.50	0.55	26.44	122.91	1.52×10^{-14}
SZ102	ob6bb9030	4.45	1.25	0.35	25.15	51.72	2.25×10^{-14}
T Tau	o63l02010	4.15	10.50	0.01	3.74	61.52	9.15×10^{-14}
	o63l02020	4.13	10.25	0.01	3.87	62.16	8.87×10^{-14}
	o63l02030	4.13	10.25	0.01	4.77	59.71	9.18×10^{-14}
TWHya	o59d01020	4.50	12.25	0.07	15.99	20.25	7.24×10^{-13}
TWA3A	ob6b22030	4.28	9.25	0.62	17.28	49.52	7.19×10^{-13}
UX Tau	ob6b54030	4.40	8.75	0.32	23.34	35.72	3.10×10^{-14}

small having very similar results in most of the cases (see Table 2).

Most sources are grouped in a region with $4.1 \lesssim \log(T_e) \lesssim 4.5$ and $8 \lesssim \log(n_e) \lesssim 12$. There are three stars outside this region: DR Tau, AA Tau and SZ 102. DR Tau converged to values lying very close to the limits of the $n_e - T_e$ grid. In the case of SZ 102, the low density probably indicates that the C II] emission is dominated by an extended ionized envelope. Something similar might be occurring in AA Tau, a CTTS with a warped disc (Ménard et al. 2003) that displays very peculiar profiles in the UV emission lines (France et al. 2012; Ardila et al. 2013; Gómez de Castro 2013b). These three stars are represented in the figure as filled circles. These “unusual” values lead us to think that maybe the C II], Fe II] and Si II] lines are not formed under the same physical conditions as the other

sources. Therefore, these three stars are excluded from the following analysis.

3.3 Consistency tests

For this purpose, we have compared the observed flux in the C II] feature with the flux derived from the best fitting model for each target - including the C II] quintuplet and the unresolved Fe II]_{2328.1} and Si II]_{2329.23} lines.

The observed flux has been measured in the range 2324-2330 Å as $F_{obs} = (f - N_{pix}F_{cont})\Delta\lambda$, where F_{cont} is the continuum average flux, N_{pix} is the number of pixels in the selected window (151 pixels), f is the wavelength-integrated line flux and $\Delta\lambda$ the step in wavelength (0.04 Å). We also estimated the corresponding flux error as $\delta F = N_{pix} \cdot \Delta\lambda \cdot$

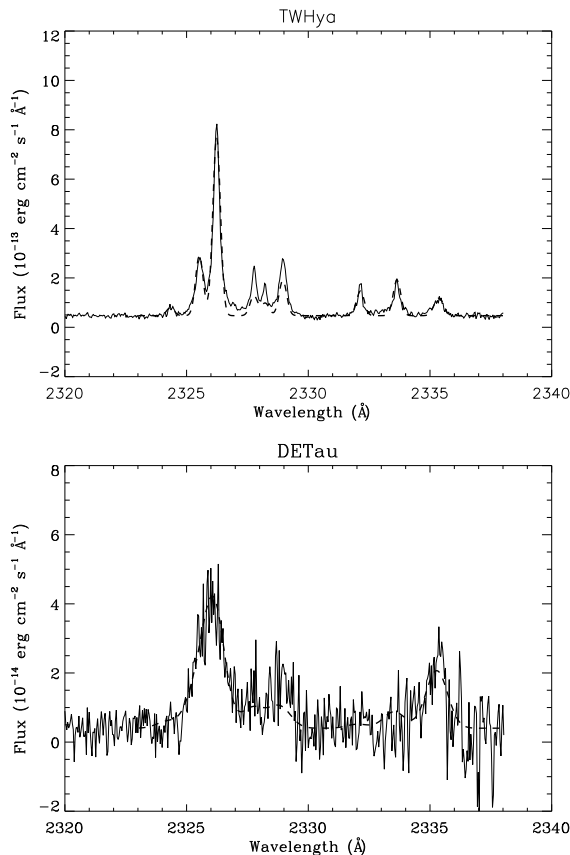


Figure 6. Original spectra (solid lines) and their best fits (dotted lines) for two example stars: TW Hya (top) and DE Tau (bottom).

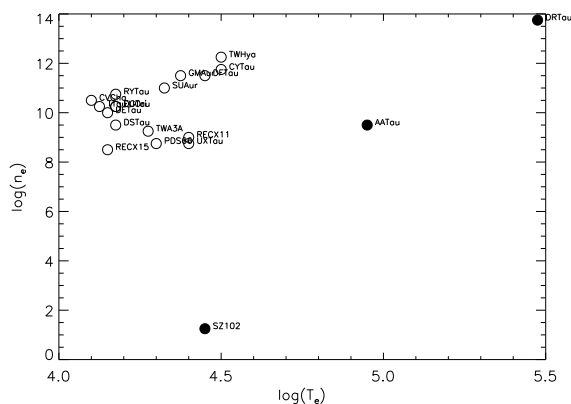


Figure 7. Electron densities (n_e in cm^{-3}) and temperatures (T_e in K) corresponding to the best fit to the observed spectra for the stars in the sample. Circle radius corresponds to the uncertainties associated with n_e and T_e . Filled circles indicate stars with values out of the range where most of the sources in the sample are present.

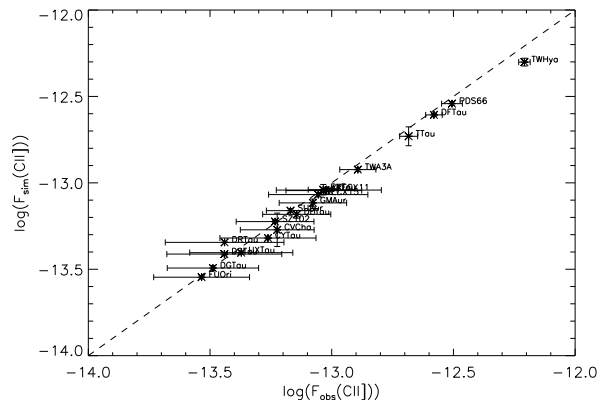


Figure 8. The observed flux in the 2326 Å feature compared with the derived from the best fit. Dashed line marks the 1:1 relation.

σ_{cont} (being σ_{cont} the dispersion around this average). The continuum was measured in the 2320-2323 Å spectral range.

The simulated flux of each line has been calculated as the integral of the Gaussian function fitting that line. Table 3 shows the fluxes for each line. The total flux of the C II] quintuplet has been calculated from the best-fitting models as

$$F_{sim}(CII) = \sigma\sqrt{2\pi}F_0 \sum_{i=0}^4 R_i \quad (2)$$

The Si II]₂₃₃₅ flux is the sum of the components at 2335.12 and 2335.52 Å since they are not resolved in the *HST*/STIS spectra.

The comparison between observed and fitted flux is shown in Fig.8. Most of the observed fluxes are slightly higher than the simulated ones but the discrepancy is well within the expected value given the S/N of the data. TW Hya shows the largest discrepancy that we interpret as a result of the simplicity of the modelling, i. e. the difficulties to fit the data to a “single plasma” emission. In this sense, we would like to remark that the (n_e, T_e) values in Table 2 should be understood as average values on the plasma emission region.

We have also calculated the contribution of the Fe II] $\lambda 2328$ and Si II] $\lambda 2329$ fluxes to the 2326 Å feature, unresolved in most of the TTSS spectra. From the simulated spectra, we have found that Fe II] $\lambda 2328$ emission can account for up to ~ 15 per cent of the flux, whereas Si II] $\lambda 2329$ contribution is negligible (≤ 0.5 per cent).

3.3.1 Line ratios as T_e and n_e indicators

The C II]/Si II] flux ratio is a sensitive tracer of the electron temperature in the range of interest. As it is shown in Fig.9, T_e is basically derived from this ratio in our code. The regression line in Fig.9 has a Pearson's coefficient of $r = 0.91$ with a p -value² = 4.8×10^{-7} . The regression equation is:

² p -value = p means that, for a random population there is $100 \cdot p$ per cent probability that the cross-correlation coefficient will be r or better. We are assuming that the correlation coefficient is statistically significant if the p -value is lower than 5 per cent.

Table 3. Fluxes of the main features derived from the fitting procedure^(a)

Star	Data set	Flux(C II)]	Flux(Fe II] ₂₃₂₈)	Flux(Si II] ₂₃₂₉) (erg s ⁻¹ cm ⁻²)	Flux(Fe II] ₂₃₃₃)	Flux(Si II] ₂₃₃₅)
AA Tau	ob6ba7030	$(9.02 \pm 0.17) \times 10^{-14}$	$(2.58 \pm 1.12) \times 10^{-20}$	$(4.59 \pm 1.42) \times 10^{-18}$	$(7.47 \pm 3.22) \times 10^{-20}$	$(4.45 \pm 1.42) \times 10^{-16}$
CV Cha	ob6b18020	$(4.84 \pm 1.02) \times 10^{-14}$	$(5.09 \pm 1.50) \times 10^{-15}$	$(1.99 \pm 0.36) \times 10^{-16}$	$(1.46 \pm 0.43) \times 10^{-14}$	$(3.52 \pm 0.59) \times 10^{-14}$
CY Tau	o5cf0302	$(4.73 \pm 0.03) \times 10^{-14}$	$(6.36 \pm 4.02) \times 10^{-16}$	$(1.52 \pm 0.22) \times 10^{-17}$	$(1.81 \pm 1.14) \times 10^{-15}$	$(3.16 \pm 0.46) \times 10^{-15}$
DE Tau	ob6ba8030	$(6.39 \pm 0.29) \times 10^{-14}$	$(1.82 \pm 0.50) \times 10^{-15}$	$(1.30 \pm 0.26) \times 10^{-16}$	$(5.21 \pm 1.44) \times 10^{-15}$	$(1.86 \pm 0.38) \times 10^{-14}$
DF Tau	o5kc0102	$(2.43 \pm 0.03) \times 10^{-13}$	$(3.75 \pm 2.34) \times 10^{-15}$	$(1.09 \pm 0.17) \times 10^{-16}$	$(1.07 \pm 0.67) \times 10^{-14}$	$(2.24 \pm 0.35) \times 10^{-14}$
DG Tau	o63l03020	$(3.13 \pm 0.09) \times 10^{-14}$	$(8.78 \pm 2.52) \times 10^{-16}$	$(5.03 \pm 0.70) \times 10^{-17}$	$(2.51 \pm 0.72) \times 10^{-15}$	$(8.03 \pm 1.26) \times 10^{-15}$
	o63l03030	$(1.48 \pm 0.13) \times 10^{-14}$	$(9.91 \pm 2.82) \times 10^{-16}$	$(7.07 \pm 1.44) \times 10^{-17}$	$(2.84 \pm 0.81) \times 10^{-15}$	$(1.01 \pm 0.21) \times 10^{-14}$
DR Tau	o63l04010	$(4.53 \pm 0.01) \times 10^{-14}$	$(3.39 \pm 2.17) \times 10^{-19}$	$(2.18 \pm 0.13) \times 10^{-17}$	$(9.94 \pm 6.35) \times 10^{-19}$	$(4.63 \pm 0.27) \times 10^{-15}$
	o63l04020	$(4.76 \pm 0.00) \times 10^{-14}$	$(3.56 \pm 2.28) \times 10^{-19}$	$(2.29 \pm 0.14) \times 10^{-17}$	$(1.05 \pm 0.67) \times 10^{-18}$	$(4.87 \pm 0.29) \times 10^{-15}$
DS Tau	o5cf01020	$(7.43 \pm 0.06) \times 10^{-14}$	$(3.73 \pm 1.13) \times 10^{-16}$	$(6.24 \pm 0.79) \times 10^{-17}$	$(1.06 \pm 0.32) \times 10^{-15}$	$(7.58 \pm 0.98) \times 10^{-15}$
	o63l08010	$(6.40 \pm 0.08) \times 10^{-14}$	$(5.91 \pm 1.06) \times 10^{-16}$	$(6.25 \pm 0.99) \times 10^{-17}$	$(1.69 \pm 0.31) \times 10^{-15}$	$(7.00 \pm 1.06) \times 10^{-15}$
	o63l08020	$(3.74 \pm 0.08) \times 10^{-14}$	$(6.49 \pm 1.08) \times 10^{-16}$	$(6.87 \pm 1.17) \times 10^{-17}$	$(1.86 \pm 0.31) \times 10^{-15}$	$(7.47 \pm 1.13) \times 10^{-15}$
FU Ori	o63l07020	$(2.77 \pm 0.06) \times 10^{-14}$	$(7.77 \pm 2.31) \times 10^{-16}$	$(4.45 \pm 0.66) \times 10^{-17}$	$(2.22 \pm 0.66) \times 10^{-15}$	$(7.11 \pm 1.18) \times 10^{-15}$
GM Aur	ob6ba1030	$(7.32 \pm 0.29) \times 10^{-14}$	$(3.31 \pm 1.84) \times 10^{-15}$	$(5.56 \pm 0.63) \times 10^{-17}$	$(9.40 \pm 5.24) \times 10^{-15}$	$(1.14 \pm 0.13) \times 10^{-14}$
PDS66	ob6b23030	$(2.85 \pm 0.06) \times 10^{-13}$	$(2.00 \pm 0.37) \times 10^{-15}$	$(3.59 \pm 0.33) \times 10^{-16}$	$(5.68 \pm 1.06) \times 10^{-15}$	$(3.15 \pm 0.27) \times 10^{-14}$
RECX15	ob6bb7030	$(8.39 \pm 0.22) \times 10^{-14}$	$(1.60 \pm 0.37) \times 10^{-15}$	$(2.19 \pm 0.46) \times 10^{-16}$	$(4.57 \pm 1.07) \times 10^{-15}$	$(1.88 \pm 0.39) \times 10^{-14}$
RECX11	ob6bc4030	$(9.06 \pm 0.13) \times 10^{-14}$	$(1.87 \pm 0.59) \times 10^{-16}$	$(6.39 \pm 0.97) \times 10^{-17}$	$(5.26 \pm 1.70) \times 10^{-16}$	$(5.83 \pm 0.88) \times 10^{-15}$
RY Tau	o63l01010	$(9.20 \pm 0.50) \times 10^{-14}$	$(2.43 \pm 0.69) \times 10^{-15}$	$(3.25 \pm 0.84) \times 10^{-16}$	$(6.96 \pm 2.00) \times 10^{-15}$	$(2.78 \pm 0.72) \times 10^{-14}$
	o63l01020	$(8.65 \pm 0.52) \times 10^{-14}$	$(4.84 \pm 1.79) \times 10^{-15}$	$(1.46 \pm 0.18) \times 10^{-16}$	$(1.38 \pm 0.51) \times 10^{-14}$	$(2.74 \pm 0.36) \times 10^{-14}$
	o63l01030	$(8.58 \pm 0.45) \times 10^{-14}$	$(5.48 \pm 2.16) \times 10^{-15}$	$(1.17 \pm 0.08) \times 10^{-16}$	$(1.56 \pm 0.62) \times 10^{-14}$	$(2.30 \pm 0.16) \times 10^{-14}$
SU Aur	o63l05010	$(6.70 \pm 0.13) \times 10^{-14}$	$(2.05 \pm 1.03) \times 10^{-15}$	$(6.29 \pm 0.59) \times 10^{-17}$	$(5.84 \pm 2.92) \times 10^{-15}$	$(1.22 \pm 0.13) \times 10^{-14}$
	o63l05020	$(6.96 \pm 0.13) \times 10^{-14}$	$(1.96 \pm 0.59) \times 10^{-15}$	$(1.12 \pm 0.17) \times 10^{-16}$	$(5.59 \pm 1.70) \times 10^{-15}$	$(1.79 \pm 0.31) \times 10^{-14}$
	ob6bb1030	$(6.09 \pm 0.26) \times 10^{-14}$	$(2.32 \pm 0.78) \times 10^{-15}$	$(9.91 \pm 1.32) \times 10^{-17}$	$(6.64 \pm 2.22) \times 10^{-15}$	$(1.73 \pm 0.26) \times 10^{-14}$
SZ102	ob6bb9030	$(5.97 \pm 0.08) \times 10^{-14}$	$(2.02 \pm 0.67) \times 10^{-18}$	$(3.67 \pm 0.60) \times 10^{-17}$	$(1.44 \pm 0.47) \times 10^{-17}$	$(1.94 \pm 0.32) \times 10^{-15}$
T Tau	o63l02010	$(1.83 \pm 0.13) \times 10^{-13}$	$(8.89 \pm 3.09) \times 10^{-15}$	$(3.70 \pm 0.64) \times 10^{-16}$	$(2.55 \pm 0.89) \times 10^{-14}$	$(6.49 \pm 1.18) \times 10^{-14}$
	o63l02020	$(1.78 \pm 0.20) \times 10^{-13}$	$(8.89 \pm 2.72) \times 10^{-15}$	$(4.81 \pm 0.99) \times 10^{-16}$	$(2.55 \pm 0.78) \times 10^{-14}$	$(7.75 \pm 1.58) \times 10^{-14}$
	o63l02030	$(1.77 \pm 0.20) \times 10^{-13}$	$(8.83 \pm 2.70) \times 10^{-15}$	$(4.78 \pm 0.98) \times 10^{-16}$	$(2.53 \pm 0.78) \times 10^{-14}$	$(7.69 \pm 1.56) \times 10^{-14}$
TWA3A	ob6b22030	$(1.18 \pm 0.03) \times 10^{-13}$	$(1.07 \pm 0.16) \times 10^{-15}$	$(1.53 \pm 0.14) \times 10^{-16}$	$(3.04 \pm 0.45) \times 10^{-15}$	$(1.52 \pm 0.11) \times 10^{-14}$
TW Hya	o59d01020	$(4.80 \pm 0.19) \times 10^{-13}$	$(1.99 \pm 1.14) \times 10^{-14}$	$(1.61 \pm 0.20) \times 10^{-16}$	$(5.65 \pm 3.25) \times 10^{-14}$	$(3.39 \pm 0.43) \times 10^{-14}$
UX Tau	ob6b54030	$(3.94 \pm 0.07) \times 10^{-14}$	$(7.86 \pm 2.54) \times 10^{-17}$	$(2.83 \pm 0.43) \times 10^{-17}$	$(2.23 \pm 0.72) \times 10^{-16}$	$(2.47 \pm 0.37) \times 10^{-15}$

^(a) Fluxes are not extinction corrected.

$$\log(F(\text{CII}]/F(\text{SiII}])) = (2.1 \pm 0.3) \log(T_e) - (8.1 \pm 1.1) \quad (3)$$

We have not found any significant correlation between C II]/Fe II]₂₃₃₃ flux ratio and the temperature.

Regarding electron density, we have recovered the expected relation between n_e and the C II]/Fe II]₂₃₃₃ and Si II]/Fe II]₂₃₃₃ ratios. The regression parameters are:

- For C II]/Fe II]₂₃₃₃: $r = -0.6$ and p -value = 0.015
 - For Si II]/Fe II]₂₃₃₃: $r = -0.9$, p -value = 8.34×10^{-7}
- and regression equation: $\log(F(\text{SiII}]/F(\text{FeII}])) = (-0.25 \pm 0.03) \log(n_e) + (3.02 \pm 0.32)$, as shown in Fig.10.

4 C II] AS AN ACCRETION TRACER

The C II] quintuplet have been found to be a good tracer of the accretion rate (Calvet et al. 2004; Ingleby et al. 2013). In this section, we discuss this point as well as the relationship between the obtained results, (n_e , T_e , σ) and accretion rate (\dot{M}).

4.1 Dispersion versus electron temperature

Further insight on the source of the profile broadening can be drawn from Fig.11. The line dispersions that best fit the observed spectra are shown in Table 2 and they are in the range $20 \lesssim \sigma \lesssim 160 \text{ km s}^{-1}$. TW Hya and CY Tau have

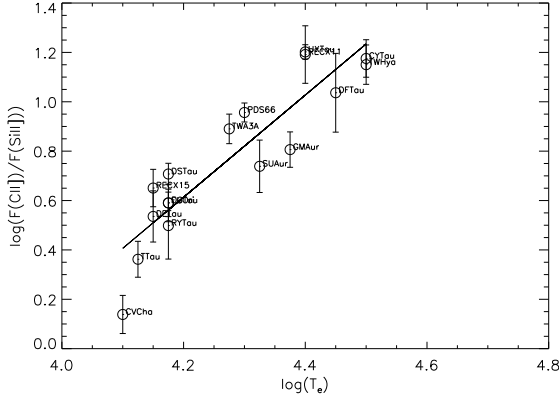


Figure 9. The ratio between C II] and Si II] fluxes $F(\text{CII]})/F(\text{SiII])}$ as a function of the temperature T_e (K). Solid line is the best linear fit.

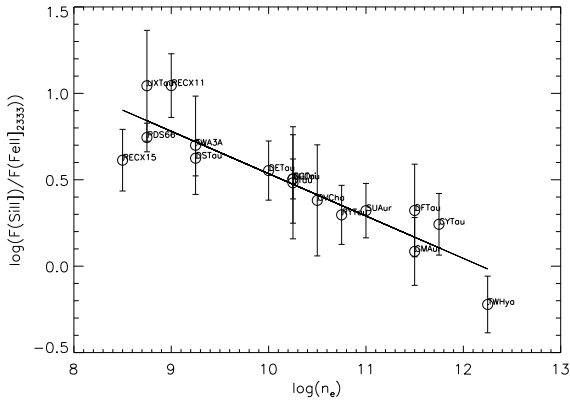


Figure 10. $F(\text{SiII]})/F(\text{FeII])}$ as a function of the electron density n_e (cm^{-3}). Solid line represents the best linear fit.

$\sigma < 25 \text{ km s}^{-1}$ and high T_e values ($\log T_e(\text{K}) \simeq 4.4 - 4.5$). For these stars the line broadening is consistent with thermal broadening ($v_{th} \sim 22 \text{ km s}^{-1}$). SU Aur is the source with the largest line broadening, $\sigma > 100 \text{ km s}^{-1}$, and a temperature of $T_e \simeq 10^{4.3} \text{ K}$. This star is the fastest rotator in the sample ($v \sin i \sim 60 \text{ km s}^{-1}$) thus, rotation could be an important source of line broadening. The rest of the stars have intermediate σ values ($40 \lesssim \sigma \lesssim 100 \text{ km s}^{-1}$) and temperatures in the range $\log T_e(\text{K}) \simeq 4.1 - 4.45$. The dispersions are suprathermal and the contribution of rotational broadening is negligible since with $v \sin i$ values are in the range $\sim 5 - 25 \text{ km s}^{-1}$ (see Table 4). There is a mild correlation between σ and T_e , as shown in Fig.11 ($r = -0.6$ and a p -value = 0.018).

4.2 Dispersion versus accretion rate

We have also examined the relation between dispersion, σ and accretion rate, \dot{M} . As shown in Fig.12, TTSs show a statistically significant correlation between σ and \dot{M} : the higher the accretion rate the wider the line. Note that there is a small group of TTSs (TWA 3A, RECX 11, RECX 15 and PDS 66) with $\dot{M} < 10^{-9} \text{ M}_{\odot} \text{ yr}^{-1}$, that seem to have

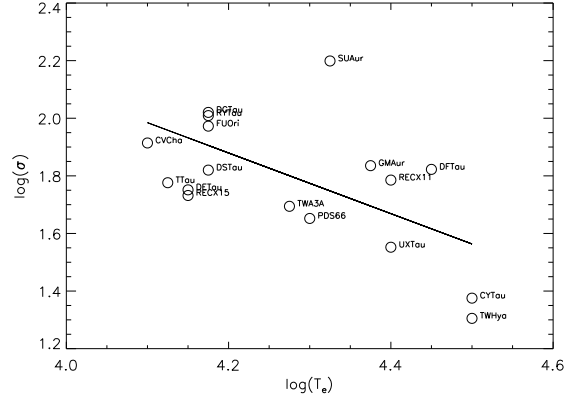


Figure 11. Line dispersion σ (km s^{-1}) as a function of temperature T_e (K). Solid line is the best linear fit. The error bars for $\log(\sigma)$ are smaller than the circle size.

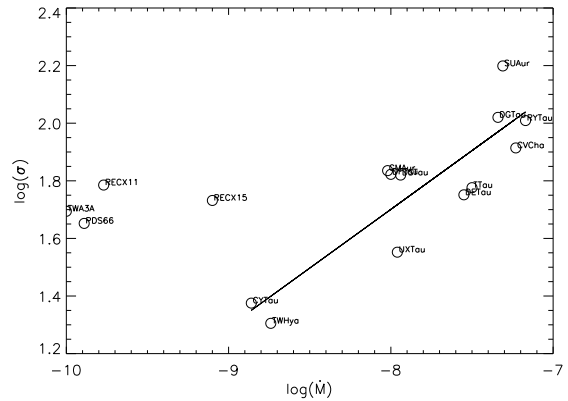


Figure 12. The calculated line width σ (km s^{-1}) as a function of the stellar accretion rate \dot{M} ($\text{M}_{\odot} \text{ yr}^{-1}$) (taken from the literature). Solid line is the best linear fit for stars with $\dot{M} \geq 10^{-9} \text{ M}_{\odot} \text{ yr}^{-1}$. The error bars for $\log(\sigma)$ are smaller than the circle size.

too low accretion rates for the given dispersion. PDS 66 also displays an unusually high C II] flux for the accretion rate derived by Ingleby et al. (2013). For this reason these stars have not been considered to determine the correlation coefficient. The Pearson's coefficient is $r = 0.87$ with a p -value = 0.0002. This trend suggests a clear connection between the region in which lines are formed and the accretion process and agrees with those trends reported recently for other UV spectral tracers (Ardila et al. 2013; Gómez de Castro 2013b).

4.3 C II] luminosity versus accretion rate

Here we re-examine the correlation reported by Ingleby et al. (2013) from low-dispersion data between the accretion rate/luminosity and the C II] flux. Fluxes are extinction corrected according to Valencic et al. (2004) assuming $R_V = 3.1$ (see Table 4 for a compilation of the A_V values and distances used in the calculation, as well as other relevant parameters). The extinction A_V is one of the

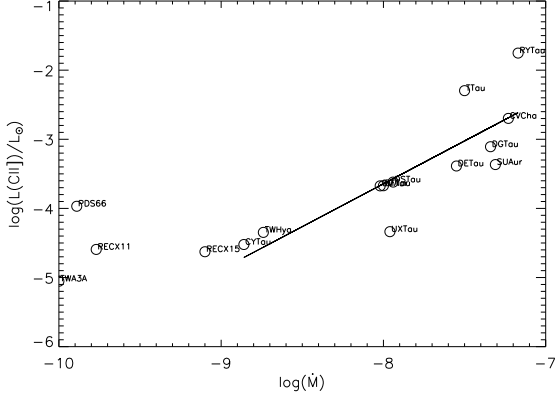


Figure 13. The C II] luminosity (in L_{\odot}) as a function of the accretion rate ($M_{\odot} \text{ yr}^{-1}$). Solid line is the best linear fit for stars with $\dot{M} \geq 10^9 M_{\odot} \text{ yr}^{-1}$.

major sources of uncertainty affecting, among other things, the accretion rate estimates. For this reason, extinctions have been selected mainly from the same source than the accretion rates (Ingleby et al. 2013). As a test, we have repeated the analysis with data from Ardila et al. (2013), and found the same general trend. As shown in Fig.13, the C II] luminosity increases as the accretion rate does:

$$\log(L(\text{CII}))/L_{\odot} = (1.24 \pm 0.26) \log \dot{M} + (6.27 \pm 2.06) \quad (4)$$

with a Pearson's correlation coefficient of $r = 0.83$ (p -value = 0.0008). This correlation is for stars with $\dot{M} > 10^{-9} M_{\odot} \text{ yr}^{-1}$. For comparison, Ingleby et al. (2013) obtain a slope $\simeq 0.9 \pm 0.2$ from low-dispersion data.

4.4 Electron density versus accretion rate

In Fig.14 we have plotted the electron density as a function of the accretion rate. TWA 3A, RECX 11, RECX 15 and PDS 66 have again a peculiar behaviour related with their, apparently, too low accretion rates when compared with the observed electron density in the emission region. There are four stars (TW Hya, CY Tau, GM Aur and DF Tau) with $n_e > 10^{11} \text{ cm}^{-3}$. There seems to be a trend for n_e to increase as the accretion rate does it ($r = 0.92$ and a p -value = 0.001) in sources with $n_e \lesssim 10^{11} \text{ cm}^{-3}$ and $\dot{M} > 10^{-8} (M_{\odot} \text{ yr}^{-1})$.

4.5 Blueshifted profiles

The shift of the lines, δ , obtained from the fitting, was corrected to the stellar rest frame and it is provided in Table 2; the radial velocities of the TTSs are compiled in Table 4. Note that the pointing errors in the STIS data result in a velocity uncertainty of 3 km s^{-1} , negligible for the purpose of this work. Most TTSs satisfy $-20 \lesssim \delta \lesssim 20 \text{ km s}^{-1}$; however, there are three stars namely, DG Tau, FU Ori and RY Tau with clearly blueshifted emission at velocities of -81.5 , -73.5 and -47.1 km s^{-1} , respectively. This blueshift indicates a contribution from the unresolved base of the jet.

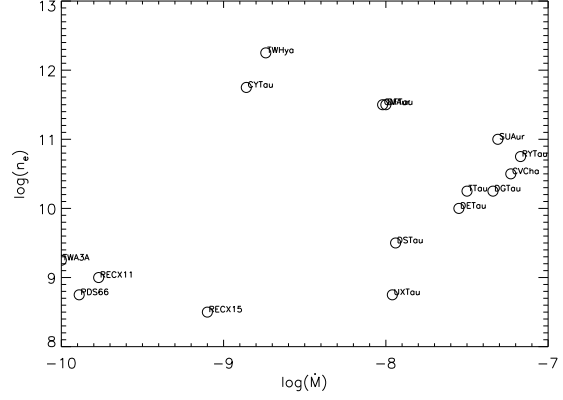


Figure 14. Electron density $n_e \text{ (cm}^{-3}\text{)}$ as a function of the accretion rate $\dot{M} (M_{\odot} \text{ yr}^{-1})$.

5 CONCLUSIONS

In this work, we have studied the semiforbidden lines of C II], Si II] and Fe II] in the 2310-2340 Å spectral range for a sample of 20 TTSs using 30 medium resolution spectra obtained with *HST*/STIS instrument.

As the lines are blended in a broad feature in most sources, we have developed a numerical method to determine the properties of the line emission region assuming that the radiating plasma can be characterized by a single T_e and n_e pair, considering solar abundances. This is the first work where n_e and T_e has been determined for such a large sample of TTSs; previous works dealt with much smaller samples (Gómez de Castro & Verdugo 2001, 2003).

In magnetospheric accretion, matter flows from the inner border of the circumstellar disc on the magnetospheric surface to finally fall on to the star. Near the stellar surface a dense and hot shock is formed producing hot spots. The sheared magnetosphere-disc boundary layer is expected to be very prone to the development of turbulent flows.

Within this overall picture there are four issues worth remarking.

- In most TTSs, the C II], Si II] and Fe II] radiation seems to be produced in an extended magnetospheric structure characterized by $10^8 \lesssim n_e \lesssim 10^{12} \text{ cm}^{-3}$ and $10^{4.1} \lesssim T_e \lesssim 10^{4.5} \text{ K}$. The line broadening is suprathermal except for two stars (TW Hya and CY Tau). The dispersion depends on the electron temperature of the radiating plasma and on the accretion rate, suggesting a connection between the line formation region and the accretion process. This is consistent with the line radiation being dominated by the magnetospheric accretion flow, close to the disc. For TW Hya and CY Tau, the densities and temperatures are higher than for the rest of the stars and similar to the observed in atmospheres of cool stars (Brown et al. 1984; Brooks et al. 2001). Also, the line broadening is thermal. Therefore, the observed emission lines in TW Hya and CY Tau are formed in a different region in the magnetospheric accretion flow (likely close to the star). In good agreement with this picture, the density and temperature in the line formation region are below the theoretical predictions for the density and temperature in the accretion shock ($n_e \simeq 10^{13} \text{ cm}^{-3}$ and $T_e \simeq 10^6 \text{ K}$) and about the densities and temperatures expected in the funnel flow

Table 4. Properties of the sample taken from the literature.

Star	SpT	L (L_{\odot})	R (R_{\odot})	M (M_{\odot})	d (pc)	$\log(\dot{M})$ ($M_{\odot} \text{ yr}^{-1}$)	$v \sin i$ (km s^{-1})	A_V (mag)	v_{rad} (km s^{-1})	Ref.
AA Tau	K7	1	2.1	0.8	140	-7.82	11	1.9	16.1	1,17
CY Tau	M2	0.31	1.63	0.55	140	-8.86	10.6	0.03	19.1	2,5,3,18
CV Cha	G9	3.1	2	1.5	160	-7.23	32	1.5	16.1	1,3,10
DE Tau	M2	0.8	2.4	0.4	140	-7.55	10	0.9	14.9	1,9,17
DF TauA	M1	0.56	3.37	0.68	140	-8	16.1	0.15	11	2,7,3,9
DG Tau	K6	1.15	1	0.88	140	-7.34	20	1.41	15.4	2,7,10,18
DR Tau	K5	0.4	1.1	0.9	140	-7.28	10	1.4	27.6	1,3,10
DS Tau	K5	0.68	1.36	1.04	140	-7.94	10	0.9	16.3	2,7,17
FU Ori	G0	—	—	—	450	—	—	—	28	15,19
GM Aur	K7	1.2	2.3	0.8	140	-8.02	12.4	0.6	15	1,9,17
PDS66	K1	0.9	1.3	1.1	86	-9.89	14	0.2	11.6	1,3,14
RECX15	M3	0.1	0.9	0.3	97	-9.1	15.9	0	15.9	1,3,13
RECX11	K5	0.6	1.4	1	97	-9.77	16.4	0	18	1,3,12
RY Tau	G1	9.6	2.9	2	140	-7.17	48.7	2.2	16.5	7,17
SU Aur	G1	7.8	2.6	1.7	140	-7.31	59	0.9	16	7,17,18
SZ102	K0	—	—	0.75	200	-8.1	—	0.32	5	3,4
T Tau	K0	7.29	2.9	2.11	140	-7.5	20.1	1.46	19.1	2,8,17
TW Hya	K7	0.3	1.1	0.8	56	-8.74	5.8	0	13.5	1,3,16
TWA3A	M3	0.4	1.8	0.3	50	-10	12	0	—	1,14
UX TauA	K5	0.91	2.05	1.09	140	-7.96	25.4	0.26	15.6	2,3,6,11,17

- (1) Ingleby et al. (2013); (2) White & Ghez (2001); (3) Ardila et al. (2013); (4) France et al. (2012); (5) Gullbring et al. (1998)
(6) Andrews et al. (2011); (7) Salyk et al. (2013); (8) Calvet et al. (2004); (9) Clarke & Bouvier (2000); (10) Johns-Krull et al. (2000);
(11) Preibisch & Smith (1997); (12) Jayawardhana et al. (2006); (13) Woitke et al. (2011); (14) da Silva et al. (2009);
(15) Petrov & Herbig (2008); (16) Herczeg et al. (2006); (17) Hartmann et al. (1986); (18) Nguyen et al. (2012);
(19) Malaroda et al. (2006).

($n_e \simeq 10^9 - 10^{12} \text{ cm}^{-3}$ and $T_e \simeq 5 \times 10^3 - 10^{4.5} \text{ K}$; see for example Calvet & Gullbring 1998; Muzerolle et al. 2001).

- There are three sources, DG Tau, FU Ori and RY Tau with blueshifted lines centroid. DG Tau and RY Tau have resolved jets and FU Ori has a strong wind. The large blueshifted velocities in these stars can be due to the contribution of the outflows to the C II] lines, suggesting that the properties in the base of the outflow are similar to those in the base of the accretion stream. The electron densities of the jet sources derived from the C II], Si II] and Fe II] lines agree well with previous estimates of electron densities at the base of the jet (Gómez de Castro & Verdugo 2001, 2003, 2007). The observations agree with the predictions of hot disc winds (Gómez de Castro & Ferro-Fontán 2005). From the theoretical point of view, it is expected that both, the base of the jet and the foot-point of the accretion flow, share similar physical conditions (see e.g. Mohanty & Shu 2008).

- The C II] quintuplet can be used as a reliable tracer of the mass accretion rate on the star. C II] luminosity increases as the accretion rate does it in agreement with previous results by Calvet et al. (2004); Ingleby et al. (2013).

ACKNOWLEDGEMENTS

The authors acknowledge support from the Spanish Ministry of Economy and Competitiveness through grant AYA2011-29754-C03-01. We also wish to thank an anonymous referee for her/his useful comments.

REFERENCES

- Andrews, S. M., Wilner, D. J., Espaillat, C., et al. 2011, *ApJ*, 732, 42
Ardila, D. R., Basri, G., Walter, F. M., Valenti, J. A., & Johns-Krull, C. M. 2002a, *ApJ*, 566, 1100
Ardila, D. R., Basri, G., Walter, F. M., Valenti, J. A., & Johns-Krull, C. M. 2002b, *ApJ*, 567, 1013
Ardila, D. R., Herczeg, G. J., Gregory, S. G., et al. 2013, *ApJS*, 207, 1
Bary, J. S., Weintraub, D. A., Shukla, S. J., Leisenring, J. M., & Kastner, J. H. 2008, *ApJ*, 678, 1088
Bouvier, J., Alencar, S. H. P., Harries, T. J., Johns-Krull, C. M., & Romanova, M. M. 2007, *Protostars and Planets V*, 479
Brooks, D. H., Costa, V. M., Lago, M. T. V. T., & Lanzafame, A. C. 2001, *MNRAS*, 327, 177
Brown, A., de M. Ferraz, M. C., & Jordan, C. 1984, *MNRAS*, 207, 831
Calvet, N., & Gullbring, E. 1998, *ApJ*, 509, 802
Calvet, N., Muzerolle, J., Briceño, C., et al. 2004, *AJ*, 128, 1294
Clarke, C. J., & Bouvier, J. 2000, *MNRAS*, 319, 457
Coffey, D., Bacciotti, F., & Podio, L. 2008, *ApJ*, 689, 1112
Comerón, F., & Fernández, M. 2011, *A&A*, 528, A99
Correia, S., Zinnecker, H., Ratzka, T., & Sterzik, M. F. 2006, *A&A*, 459, 909
da Silva, L., Torres, C. A. O., de La Reza, R., et al. 2009, *A&A*, 508, 833
Dere, K. P., Landi, E., Mason, H. E., Monsignori Fossi, B. C., & Young, P. R. 1997, *A&AS*, 125, 149
Espaillat, C., D'Alessio, P., Hernández, J., et al. 2010, *ApJ*, 717, 441

- France, K., Schindhelm, E., Herczeg, G. J., et al. 2012, *ApJ*, 756, 171
- Furlan, E., Hartmann, L., Calvet, N., et al. 2006, *ApJS*, 165, 568
- Gómez de Castro, A. I. 2013a, *Planets, Stars and Stellar Systems. Volume 4: Stellar Structure and Evolution*, 279
- Gómez de Castro, A. I. 2013b, *ApJ*, 775, 131
- Gómez de Castro, A. I., & Ferro-Fontán, C. 2005, *MNRAS*, 362, 569
- Gómez de Castro, A. I., & Marcos-Arenal, P. 2012, *ApJ*, 749, 190
- Gómez de Castro, A. I., & Verdugo, E. 2001, *ApJ*, 548, 976
- Gómez de Castro, A. I., & Verdugo, E. 2003, *ApJ*, 597, 443
- Gómez de Castro, A. I., & Verdugo, E. 2007, *ApJL*, 654, L91
- Guenther, E. W., Esposito, M., Mundt, R., et al. 2007, *A&A*, 467, 1147
- Gullbring, E., Hartmann, L., Briceno, C., & Calvet, N. 1998, *ApJ*, 492, 323
- Hartmann, L., Hewett, R., Stahler, S., & Mathieu, R. D. 1986, *ApJ*, 309, 275
- Hayes, M. A., & Nussbaumer, H. 1984a, *A&A*, 134, 193
- Hayes, M. A., & Nussbaumer, H. 1984b, *A&A*, 139, 233
- Herczeg, G. J., Linsky, J. L., Walter, F. M., Gahm, G. F., & Johns-Krull, C. M. 2006, *ApJs*, 165, 256
- Howard, C. D., Sandell, G., Vacca, W. D., et al. 2013, *ApJ*, 776, 21
- Ingleby, L., Calvet, N., Herczeg, G., et al. 2013, *ApJ*, 767, 112
- Ingleby, L., Calvet, N., Hernández, J., et al. 2011, *AJ*, 141, 127
- Jayawardhana, R., Coffey, J., Scholz, A., Brandeker, A., & van Kerkwijk, M. H. 2006, *ApJ*, 648, 1206
- Johns-Krull, C. M., Valenti, J. A., & Linsky, J. L. 2000, *ApJ*, 539, 815
- Keenan, F. P., Lennon, D. J., Johnson, C. T., & Kingston, A. E. 1986, *MNRAS*, 220, 571
- Koenigl, A. 1991, *ApJL*, 370, L39
- Kravtsova, A. S., & Lamzin, S. A. 2002, *Astronomy Letters*, 28, 676
- Kulkarni, A. K., & Romanova, M. M. 2013, *MNRAS*, 433, 3048
- Kurosawa, R., & Romanova, M. M. 2013, *MNRAS*, 431, 2673
- Lamzin, S. A. 2000, *Astronomy Letters*, 26, 225
- Landi, E., Young, P. R., Dere, K. P., Del Zanna, G., & Mason, H. E. 2013, *ApJ*, 763, 86
- Malaroda, S., Levato, H., & Galliani, S. 2006, *VizieR Online Data Catalog*, 3249, 0
- Ménard, F., Bouvier, J., Dougados, C., Mel'nikov, S. Y., & Grankin, K. N. 2003, *A&A*, 409, 163
- Mohanty, S., & Shu, F. H. 2008, *ApJ*, 687, 1323
- Muzerolle, J., Calvet, N., & Hartmann, L. 2001, *ApJ*, 550, 944
- Nguyen, D. C., Brandeker, A., van Kerkwijk, M. H., & Jayawardhana, R. 2012, *ApJ*, 745, 119
- Petrov, P. P., & Herbig, G. H. 2008, *AJ*, 136, 676
- Preibisch, T., & Smith, M. D. 1997, *A&A*, 322, 825
- Romanova, M. M., Ustyugova, G. V., Koldoba, A. V., & Lovelace, R. V. E. 2012, *MNRAS*, 421, 63
- Salyk, C., Herczeg, G. J., Brown, J. M., et al. 2013, *ApJ*, 769, 21
- Stencel, R. E., Linsky, J. L., Brown, A., et al. 1981, *MNRAS*, 196, 47P
- St-Onge, G., & Bastien, P. 2008, *ApJ*, 674, 1032
- Uchida, Y., & Shibata, K. 1984, *PASJ*, 36, 105
- Unruh, Y. C., Collier Cameron, A., & Guenther, E. 1998, *MNRAS*, 295, 781
- Valencic, L. A., Clayton, G. C., & Gordon, K. D. 2004, *ApJ*, 616, 912
- Wang, H., Apai, D., Henning, T., & Pascucci, I. 2004, *ApJL*, 601, L83
- White, R. J., & Ghez, A. M. 2001, *ApJ*, 556, 265
- Woitke, P., Riaz, B., Duchêne, G., et al. 2011, *A&A*, 534, A44
- Yang, H., Herczeg, G. J., Linsky, J. L., et al. 2012, *ApJ*, 744, 121

APPENDIX A: VARIABILITY OF THE C II] PROFILES

Significant variations in the C II] profiles are only found in DS Tau (see Fig.A1). In this section, we include the figures showing the variability of the C II] profiles in TTSs. Only observations with $S/N > 2$ are compared.

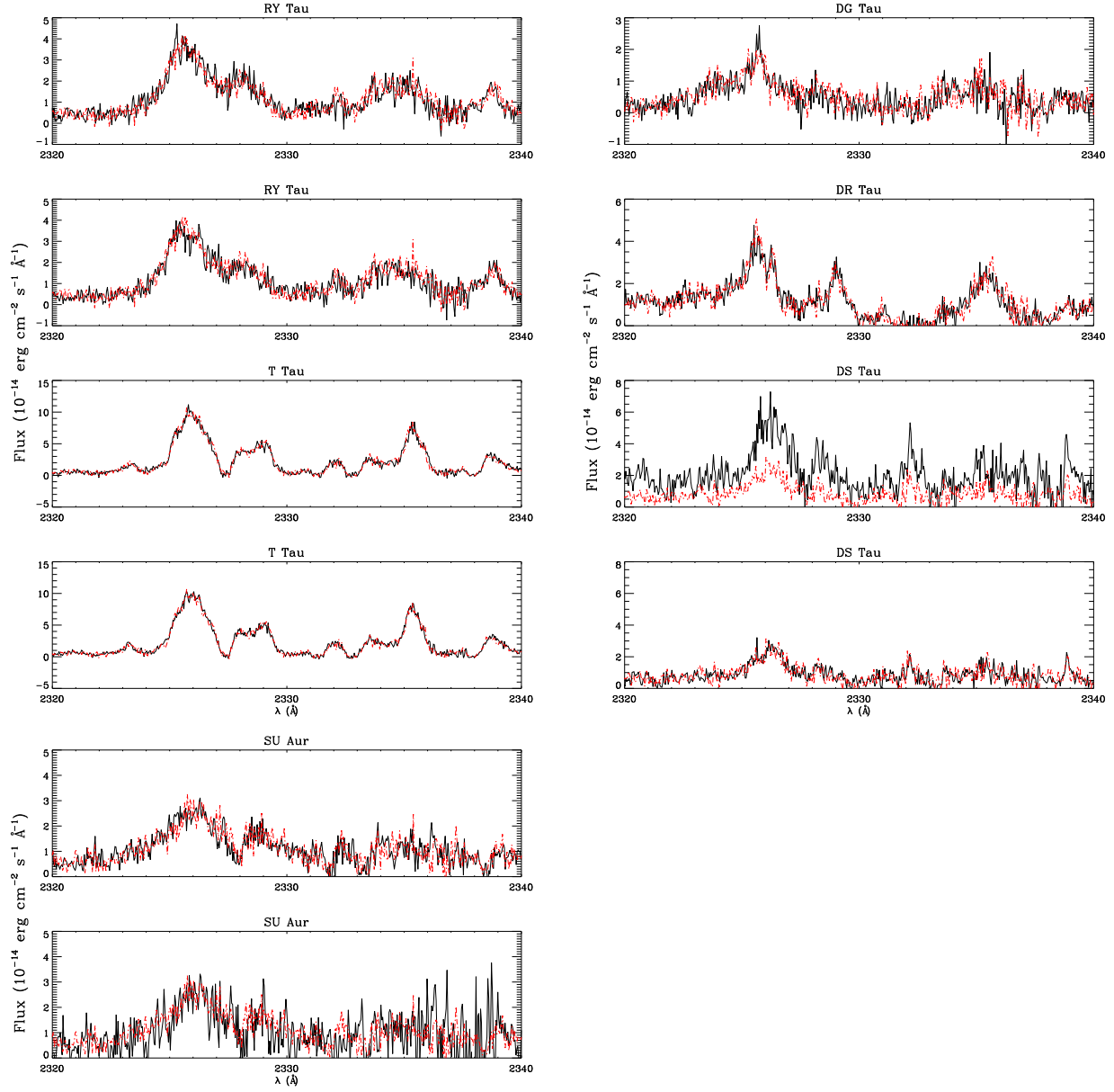


Figure A1. Variability of the C II profiles of the TTSS. For each star, the highest S/N observation is used as reference and is superimposed as red dotted line.